Boltzmann equation simulation for a trapped Fermi gas of atoms

Boltzmann equation simulation for a trapped Fermi gas of atoms

O Goulko[1,4,5]**, F Chevy**[2] **and C Lobo**[3]

[1] Department of Applied Mathematics and Theoretical Physics, University of Cambridge, Centre for Mathematical Sciences, Cambridge CB3 0WA, UK
[2] Laboratoire Kastler Brossel, Ecole Normale Supérieure, CNRS, UPMC, 24 rue Lhomond, 75231 Paris Cedex 05, France
[3] School of Mathematics, University of Southampton, Highfield, Southampton SO17 1BJ, UK
E-mail: O.Goulko@physik.uni-muenchen.de

Abstract. The dynamics of an interacting Fermi gas of atoms at sufficiently high temperatures can be efficiently studied via a numerical simulation of the Boltzmann equation. In this paper, we describe in detail the setup we used recently to study the oscillations of two spin-polarized fermionic clouds in a trap. We focus here on the evaluation of interparticle interactions. We compare different ways of choosing the phase space coordinates of a pair of atoms after a successful collision and demonstrate that the exact microscopic setup has no influence on the macroscopic outcome.

[4] Author to whom any correspondence should be addressed.
[5] Present address: Physics Department, Arnold Sommerfeld Center for Theoretical Physics and Center for NanoScience, Ludwig-Maximilians-Universität, Theresienstraße 37, 80333 Munich, Germany.

IOP Institute of Physics ⦿ DEUTSCHE PHYSIKALISCHE GESELLSCHAFT

Contents

1. Introduction

The Boltzmann simulation of the semiclassical regime of trapped Fermi gases [1] has become a crucial tool for understanding recent experiments [2–5] where spin-polarized atomic clouds undergo strong collisions. This simulation is one of the very few methods that allow us to calculate accurately, e.g., spin transport coefficients in ways that can then be quantitatively compared with experiments. In a previous work [6], we studied the collision of two spin-polarized fermionic clouds and obtained excellent agreement with experimental results. The goal of this paper is to describe in detail the numerical setup that was used there and to present tests of the simulation and other information that will be potentially very useful for those wishing to implement this important method.

Our setup is related to that of Lepers *et al* [7], but we have introduced several new modifications [8]. For instance, we placed an artificial grid over the continuous coordinate space that allows us to evaluate particle collisions efficiently. However, the main difference between [7] and this work lies in the method used to choose the new positions and momenta of two colliding particles after the collision. A quantum mechanical collision is a fundamentally random process with constraints given by the symmetries of the system. There are several ways of implementing these constraints within the framework of a molecular dynamics simulation. We will discuss the physics of several collisional setups, and compare the numerical results associated with them in detail. We find that, although they exhibit very similar macroscopic behaviour, there are distinct technical advantages that make some of the methods preferable to the others.

In section 2 of this paper, we introduce the general numerical setup. We describe the method of test particles and explain the conditions that need to be fulfilled for a semiclassical collision to take place and how to efficiently search the system for suitable collision partners.

Different ways of choosing new positions and momenta after a collision are discussed in detail in section 3. In section 4, we show how to determine the optimal simulation parameters and present several tests of the numerical method, in particular the different collisional setups. A summary of our results and an outlook on future work can be found in section 5.

2. Numerical setup

2.1. Definitions

We consider a system of two-component fermions with equal mass m, labelled by the spin index $s = \{\uparrow, \downarrow\}$ and we work in units in which $\hbar = k_B = 1$. Fermions of opposite spin can interact via s-wave scattering and the cross section is given by

$$\sigma = \frac{4\pi a^2}{1 + a^2 \mathbf{p}_{rel}^2/4},\tag{1}$$

where a is the scattering length and $\mathbf{p}_{rel} = \mathbf{p}_\uparrow - \mathbf{p}_\downarrow$ is the relative momentum of the two atoms. We assume that the system is in the normal phase and that the temperature is sufficiently high, so that the two spin distributions can be described semiclassically in terms of the functions $f_s(\mathbf{r}, \mathbf{p}, t)$. Within the local density approximation the equilibrium distribution for fermions is given by the Fermi–Dirac distribution

$$f_s^{(FD)}(\mathbf{r}, \mathbf{p}) = \frac{1}{e^{(p^2/2m + V(\mathbf{r}) - \mu_s)/T} + 1},\tag{2}$$

where T is the temperature and μ_s the chemical potential defined by the normalization condition

$$N_s = N/2 = \int d^3 r\, n_s(\mathbf{r}, t) = \int d^3 r \int \frac{d^3 p}{(2\pi)^3} f_s(\mathbf{r}, \mathbf{p}, t).\tag{3}$$

The atom number for each species is assumed to be equal, $N_\uparrow = N_\downarrow = N/2$, and will be kept fixed during the simulation. The trapping potential is assumed to be harmonic,

$$V(\mathbf{r}) = \frac{1}{2}m \left(\omega_x^2 x^2 + \omega_y^2 y^2 + \omega_z^2 z^2\right),\tag{4}$$

with the three trapping frequencies ω_x, ω_y and ω_z. In the following, we will only consider the isotropic case $\omega_x = \omega_y = \omega_z$ or a cigar-shaped trap with $\omega_z < \omega_x = \omega_y \equiv \omega_\perp$. The geometric average of the trap frequencies is denoted by $\omega_0 = (\omega_x \omega_y \omega_z)^{1/3}$.

We define the Fermi energy from the energy distribution of the non-interacting gas at zero temperature, $\tilde{\varepsilon}_F = \tilde{T}_F = (3N)^{1/3}\omega_0$. This energy scale marks the frontier between the classical and quantum regimes. For $T \gtrsim \tilde{T}_F$ the fermions essentially behave like classical particles and can be described by the Maxwell–Boltzmann distribution

$$f_s^{(MB)}(\mathbf{r}, \mathbf{p}) = N_s \frac{\omega_0^3}{T^3} e^{-(p^2/2m + V(\mathbf{r}))/T}.\tag{5}$$

For $T \lesssim \tilde{T}_F$, the Fermi energy can also be used to determine the typical scales of the cloud, $\tilde{\varepsilon}_F = \tilde{k}_F^2/2m = m\omega_i^2 R_i^2/2$, where $\tilde{k}_F$ is the Fermi momentum and $R_i = \tilde{k}_F/(m\omega_i)$ are the Thomas–Fermi radii in the three spatial directions. These quantities give the widths of the zero-temperature momentum and density distributions, respectively, and are therefore useful in describing the extent of the cloud in the momentum and coordinate space.

The time evolution of the distribution function $f_s(\mathbf{r}, \mathbf{p}, t)$ is given by the Boltzmann–Uehling–Uhlenbeck equation [9], hereafter simply called the Boltzmann equation

$$\partial_t f_s + (\mathbf{p}/m) \cdot \nabla_r f_s - \nabla_r V \cdot \nabla_p f_s = -I[f_s, f_{\bar{s}}], \tag{6}$$

where the left-hand side represents the propagation of the atoms in the potential and the right-hand side stands for the collision integral, which depends on the particle statistics. Here, we consider only collisions between atoms carrying opposite spins. Indeed, for ultracold fermions, the Pauli principle forbids interactions between particles of the same spin [1]. At temperatures $T \gtrsim \tilde{T}_F$ when the Maxwell–Boltzmann distribution is applicable, the collision integral takes the form

$$I_{\text{class}}[f_s, f_{\bar{s}}] = \int \frac{\mathrm{d}^3 p_{\bar{s}}}{(2\pi)^3} \int \mathrm{d}\Omega \frac{\mathrm{d}\sigma}{\mathrm{d}\Omega} \frac{|\mathbf{p}_s - \mathbf{p}_{\bar{s}}|}{m} [f_s f_{\bar{s}} - f_s' f_{\bar{s}}'], \tag{7}$$

where the indices s and $\bar{s}$ label the two colliding atoms of opposite spin, the primed variables refer to quantities after the collision and Ω is the angle between the incoming and outgoing relative momenta. The Pauli exclusion principle only allows fermions to scatter into a previously unoccupied quantum state. This reduces the scattering probability by the Pauli blocking term proportional to $(1 - f_s')(1 - f_{\bar{s}}')$. Taking this into account, the collision integral reads

$$I[f_s, f_{\bar{s}}] = \int \frac{\mathrm{d}^3 p_{\bar{s}}}{(2\pi)^3} \int \mathrm{d}\Omega \frac{\mathrm{d}\sigma}{\mathrm{d}\Omega} \frac{|\mathbf{p}_s - \mathbf{p}_{\bar{s}}|}{m} [f_s f_{\bar{s}}(1 - f_s')(1 - f_{\bar{s}}') - f_s' f_{\bar{s}}'(1 - f_s)(1 - f_{\bar{s}})]. \tag{8}$$

At temperatures $T \gtrsim \tilde{T}_F$ the Pauli terms are close to 1 and therefore the collision integral (8) tends to the classical form (7).

2.2. Test particles

To efficiently simulate the evolution of the continuous distribution function $f_s(\mathbf{r}, \mathbf{p}, t)$, we use the method of test particles. These are point-like particles which form a discrete approximation to $f_s(\mathbf{r}, \mathbf{p}, t)$ through δ-functions. In order for this approximation to be accurate, we will represent each fermion by several test particles [7, 10, 11]. The higher the ratio $\tilde{N}/N$ of test particles to atoms, the more precisely the continuous distribution function will be approximated,

$$f_s(\mathbf{r}, \mathbf{p}, t) \to \frac{N_s}{\tilde{N}_s} \sum_{i=1}^{\tilde{N}_s} (2\pi)^3 \delta(\mathbf{r} - \mathbf{r}_i(t)) \delta(\mathbf{p} - \mathbf{p}_i(t)). \tag{9}$$

Physical observables need to be rescaled; for instance, the test particle cross section becomes $\tilde{\sigma} = \sigma(N/\tilde{N})$. A generic thermal expectation value of a single-particle observable $X(\mathbf{r}, \mathbf{p})$ can be easily calculated within the test particle picture, as the integration reduces to a sum over all test particles,

$$\langle X \rangle = \sum_s \frac{1}{N_s} \int \mathrm{d}^3 r \int \frac{\mathrm{d}^3 p}{(2\pi)^3} f_s(\mathbf{r}, \mathbf{p}, t) X(\mathbf{r}, \mathbf{p}) \tag{10}$$

$$= \frac{1}{\tilde{N}} \sum_{i=1}^{\tilde{N}} X(\mathbf{r}_i, \mathbf{p}_i). \tag{11}$$

We introduce a discrete time step Δt, such that during each time step the test particles propagate without colliding, following their classical trajectories. At the end of each time step, collisions between them are evaluated. In a harmonic potential the trajectories are given by

$$r_j(t_{n+1}) = r_j(t_n) \cos(\omega_j \Delta t) + (p_j(t_n)/m\omega_j) \sin(\omega_j \Delta t), \tag{12}$$

$$p_j(t_{n+1}) = p_j(t_n) \cos(\omega_j \Delta t) - r_j(t_n) m\omega_j \sin(\omega_j \Delta t), \tag{13}$$

where $j \in \{x, y, z\}$. Note that since the time step is fixed, the trigonometric functions only need to be evaluated once during the entire simulation, so that using the exact solution is more efficient than using the Verlet algorithm, as in for instance [7, 10], in which case the accelerations need to be recalculated for every time step. The Verlet algorithm is more general as it is applicable to any potential. But since in this work we will only consider harmonic potentials, we will use the exact solution instead.

We evaluate the probability for a two-particle collision in the same way as that described in [7]. First we must test whether a given pair of test particles reaches the point of closest approach during the present time step. This condition is important for preventing particles from attempting to collide with each other repeatedly over several consecutive time steps, an issue that will be further addressed below. If the closest approach condition is true, we check if the minimal distance $d_{\min}$ of the test particles fulfils the classical condition for scattering: $\pi d_{\min}^2 < \tilde{\sigma}$. If this condition is also satisfied, we propose a collision at the time of closest approach. However, due to Pauli statistics, even when the classical conditions for scattering are fulfilled, a collision can take place only if the new state of the particles was previously unoccupied. To take this into account we calculate the quantum mechanical scattering probability given by the Pauli term $(1 - f_s')(1 - f_{\bar{s}}')$ and accept or reject the collision according to this probability. Clearly, the point-like particle picture is unsuitable for the calculation of this probability. To return to a continuous distribution we therefore have to smear out the δ-functions representing the test particles, e.g. by Gaussians in position and momentum space:

$$\delta(\mathbf{p} - \mathbf{p}_i) \rightarrow \frac{e^{-(\mathbf{p}-\mathbf{p}_i)^2/w_p^2}}{(\sqrt{\pi} w_p)^3}, \tag{14a}$$

$$\delta(\mathbf{r} - \mathbf{r}_i) \rightarrow \frac{e^{-(x-x_i)^2/w_x^2}}{\sqrt{\pi} w_x} \frac{e^{-(y-y_i)^2/w_y^2}}{\sqrt{\pi} w_y} \frac{e^{-(z-z_i)^2/w_z^2}}{\sqrt{\pi} w_z}. \tag{14b}$$

The widths of these Gaussians, w_x, w_y, w_z and w_p, need to be tuned so that, on the one hand, fluctuations due to the discrete nature of the test particle picture are smoothed out and, on the other hand, the physical structure of the distribution function f_s remains preserved [7]. The first condition is equivalent to

$$w_p w_r \gg (N/\tilde{N})^{1/3}, \tag{15}$$

where we introduced $w_r = (w_x w_y w_z)^{1/3}$, the geometric average of the spatial widths. The second condition implies $w_i \ll R_i$ and $w_p \ll \tilde{k}_F$.

We also require that smearing by the Gaussian functions preserves the temperature-dependent degeneracy effects of the Fermi distribution, in particular close to the Fermi surface. This implies that

$$w_p \ll \tilde{k}_F(T/\tilde{T}_F) \quad \text{and} \quad w_i \ll R_i(T/\tilde{T}_F). \tag{16}$$

Note that the smearing width in momentum space is isotropic, whereas in position space the smearing width can be different, depending on the spatial direction, if the corresponding trap frequencies are unequal. Since the Thomas–Fermi radii are inversely proportional to the corresponding trap frequencies, it is sensible to choose $w_i = w_r \omega_0 / \omega_i$ for the spatial widths. Furthermore, equation (16) together with the definition of the Thomas–Fermi radii imply that $w_p = m \omega_0 w_r$. Hence, all four smearing widths can be reduced to only one free parameter. At very low temperatures the margin given by conditions (15) and (16) becomes so narrow that it is impossible to find smearing widths satisfying both conditions, without having to significantly increase the number of test particles. This limits the applicability of this setup to temperatures above approximately $0.2 \tilde{T}_F$ for $\tilde{N}/N = 10$. Moreover, at very low temperatures the system undergoes a phase transition into a superfluid state. This method does not include the relevant degrees of freedom of the superfluid Fermi gas and is applicable only in the normal phase.

2.3. Auxiliary grid

The main numerical challenge is to efficiently evaluate collisions between the test particles. The total number of pairs of opposite spin is $\tilde{N}^2/4$, which is an unfavourable scaling given that we want to use large particle numbers and a high test-particle-to-particle ratio. In this work, we develop a more efficient method than checking all possible test particle pairs. A key observation is that since the cross section decreases with increasing relative momentum it can never exceed $\tilde{\sigma}_{max} = 4\pi a^2 N/\tilde{N}$ and consequently the maximal distance two colliding test particles can have is $d_{max} = 2a\sqrt{N/\tilde{N}}$. Bearing this in mind we superpose a cubic grid with cell size d_{max} on the continuous space. The grid has finite extent which can be set by demanding that a certain proportion, for instance at least 95%, of the test particles be within the grid. For a cigar-shaped trap the grid must have a larger extent in the axial direction. At the end of each time step we move systematically through all grid cells starting in one of the corners and note all possible collision partners that fulfil the classical scattering conditions. To make sure that we do not miss collisions due to boundary effects, for each particle we check not only all opposite spin particles in the same grid cell, but also in all neighbouring cells (the ones sharing a face, an edge or a vertex with the given cell). This ensures that all particles in a sphere of radius d_{max} around a given particle are definitely accounted for. This makes a total of $3^3 = 27$ cells for each particle; however, to avoid double counting we only need to evaluate cells in the positive direction, which means on average 14 cells per particle.

A small systematic error source remains with this setup. If the relative velocity of two particles is large they can be in non-neighbouring cells at the beginning and at the end of a time step, although in the course of the time step they come within each other's allowed collision range. Such a possible collision will then not be accounted for. However, this systematic error can be minimized by choosing the time step to be sufficiently small and also by choosing the cell size to be larger than d_{max}. Also note that for large relative velocities the cross section is small and collisions between very fast particles are rare events.

After having searched the entire grid for classically allowed collision pairs we proceed to choose which collisions will indeed take place. To do so, we consecutively select random pairs from the list. We then propagate both particles to the point of their closest approach, let them scatter (the exact setup for determining the new positions and momenta after scattering is described in section 3) and then propagate them back to the original time. To account for quantum statistics we then calculate the Pauli blocking factors using the new distributions

$f'_s = f_s(\mathbf{r}', \mathbf{p}')$. The continuous distributions are obtained by replacing the δ-functions in (9) according to (14). If we obtain a value $f'_s > 1$ from the summation, we set $f'_s = 1$. The probability that the collision is accepted is then given by $(1 - f'_s)(1 - f'_{\bar{s}})$. Regardless of whether a collision is accepted or rejected, neither of the particles concerned is allowed to collide again with another particle during the present time step. If the collision is accepted we keep the new positions and momenta. If the collision is rejected we return to the values before the collision. This procedure is repeated until all possible pairs have been evaluated.

3. Collisional setup

Since the picture of colliding point-like particles with well-defined positions and momenta is a classical interpretation of a quantum mechanical scattering process, it is unsurprising that there must be some ambiguity in the implementation of the collisional setup. In the semiclassical particle picture each collision has 12 degrees of freedom: three position and three momentum components for each of the two particles, or equivalently three components of the total and relative positions and momenta. In quantum mechanics, we consider wave packets rather than particles, and concepts like particle position or momentum are not well defined. Instead, the system is described by operators which, depending on the symmetries of the system, commute with the Hamiltonian and define quantum numbers corresponding to conserved quantities. The concept of a trajectory does not exist, as a particle is not localized in phase space but rather smeared out over a certain phase space volume in accordance with Heisenberg's uncertainty principle. Therefore, in the collisional setup, it is not necessary to preserve, for instance, the exact positions of the two atoms during a collision. In the presence of an axially symmetric external potential for instance, the only conserved quantities are the total energy and the angular momentum component L_z.

3.1. Angular momentum-preserving setup

The method used in this work and in [6] can be motivated as follows. As collisions are short-ranged, we can disregard the external potential during the collision and go to the centre-of-mass frame of the two particles. Motivated by the analogue of classical scattering, we wish to conserve the total momentum, the total energy and the total angular momentum of the system during the collision. In this case the total energy is comprised only of the kinetic energy, since we always ignore mean fields, so there is no interaction energy in our setup. Conservation of the total momentum $\mathbf{p} = \mathbf{p}_s + \mathbf{p}_{\bar{s}}$ and the total energy $E = E_{\mathrm{kin}} = (p_s^2 + p_{\bar{s}}^2)/2m$ together implies the conservation of the modulus of the relative momentum $p_{\mathrm{rel}} = |\mathbf{p}_s - \mathbf{p}_{\bar{s}}|$, since $p^2 + p_{\mathrm{rel}}^2 = 2(p_s^2 + p_{\bar{s}}^2) = 4mE$. The direction of the relative momentum vector can change during the collision. Finally, we must also conserve the angular momentum $\mathbf{L} = \mathbf{r}_{\mathrm{rel}} \times \mathbf{p}_{\mathrm{rel}}$. We can satisfy all these constraints by rotating both the relative momentum and relative position vectors by the same arbitrary angle around the $\mathbf{L}$-axis. The angle of this rotation is the only degree of freedom of the collision and is determined at random. From the new values $\mathbf{p}'_{\mathrm{rel}}$ and $\mathbf{r}'_{\mathrm{rel}}$ the new values of the momenta and positions of the individual particles can be recovered using the total momentum conservation and the centre-of-mass coordinates, respectively.

So far we have ignored the external potential, which would be justified if the collisions took place when the atoms were infinitesimally close to each other and therefore experiencing the same potential. However, the two colliding particles are not at exactly the same position before

IOP Institute of Physics Φ DEUTSCHE PHYSIKALISCHE GESELLSCHAFT

the collision and their relative position changes after a successful collision. Thus, potential energy is not conserved and the total energy conservation is not exact during a collision in general. Nevertheless, we will show below that such changes in the total energy are negligibly small for almost any collision. Furthermore, these small changes cancel each other in a many-particle system which experiences many collisions.

3.2. Energy-preserving setup

It is possible to preserve energy conservation exactly by employing a different setup, as in, for instance, [7]. In [7], the relative position stays fixed during a collision and the relative momentum vector is rotated by a random angle in space (such a rotation has two degrees of freedom). As a direct consequence of the unrestricted rotation this setup violates angular momentum conservation. Although it is true that this violation would occur naturally in non-axially symmetric potentials even for non-interacting atoms, this collisional setup provides an additional, unphysical change of angular momentum. At any rate, since in this work we consider either isotropic or axially symmetric potentials, either the total angular momentum or its axial component L_z is conserved.

4. Tests and optimal parameters

How accurately the numerical setup represents the physical picture depends crucially on the values of the simulation parameters, in particular $\tilde{N}/N$, the time step Δt and the smearing widths w_r and w_p. For all tests described below we use $N = 10\,000$ atoms and $\tilde{N}/N = 10$, which is sufficient for temperatures $T \geqslant 0.2\tilde{T}_\mathrm{F}$.

The optimal value of Δt depends on the physical parameters of the system. Obvious requirements are that the time step must be smaller than the typical time between two collisions and that the average distance travelled during a time step must be much smaller than the diameter of the cross section, $\langle v_\mathrm{rel} \rangle \Delta t \ll \sqrt{\langle \tilde{\sigma} \rangle / \pi}$. Another constraint is that the time step must be smaller than the half-period with respect to the largest trap frequency, $\Delta t < \pi/\omega_\mathrm{max}$, but unless the aspect ratio is very large this condition is much weaker than the others. There is no lower bound on the time step; however, the simulation slows down with decreasing Δt.

We first describe the tuning of the parameters and the corresponding tests of the simulation with the angular momentum-preserving collisional setup 3.1. We perform the same tests as in [7] to demonstrate that even with different collisional setups we obtain very good agreement. Then we explicitly compare the different collisional setups in section 4.4.

4.1. Equilibrium collision rates

To obtain the correct dynamical properties, for instance the damping time of excitation modes, we need to ensure that the equilibrium collision rate observed in the simulation corresponds to the correct theoretical value. The number of collisions in a given time interval can be very easily obtained from the simulation, simply by counting all test particle collisions and then multiplying by the ratio $(N/\tilde{N})$. The theoretical value for the collision rate γ in the presence of Pauli blocking is given by the following integral:

$$\gamma_\mathrm{block} = \int \mathrm{d}^3 r \int \frac{\mathrm{d}^3 p_s}{(2\pi)^3} \int \frac{\mathrm{d}^3 p_{\bar{s}}}{(2\pi)^3} \int \mathrm{d}\Omega \frac{\mathrm{d}\sigma}{\mathrm{d}\Omega} |\mathbf{p}_s - \mathbf{p}_{\bar{s}}| f_s f_{\bar{s}} (1 - f'_s)(1 - f'_{\bar{s}}). \tag{17}$$

After inserting the Fermi–Dirac distribution this integral can be calculated numerically [7]. The numerical setup also provides a powerful tool for artificially switching off Pauli blocking. This allows us to separately check for errors related to the general numerical setup and the calculation of the Pauli blocking factors. Without Pauli blocking the integral is simpler and can be solved analytically for the Maxwell–Boltzmann distribution

$$\gamma_{\text{noblock}} = \int d^3r \int \frac{d^3 p_s}{(2\pi)^3} \int \frac{d^3 p_{\bar{s}}}{(2\pi)^3} \int d\Omega \frac{d\sigma}{d\Omega} |\mathbf{p}_s - \mathbf{p}_{\bar{s}}| f_s f_{\bar{s}} \tag{18}$$

$$= N_\uparrow N_\downarrow \frac{2\omega_0^3}{\pi T^2} \left(1 + \frac{1}{ma^2T} e^{\frac{1}{ma^2T}} \text{Ei} \left(-\frac{1}{ma^2T} \right) \right), \tag{19}$$

where $\text{Ei}(x) = \int_{-\infty}^{x} (e^t/t) dt$ is the exponential integral. Furthermore, we can obtain the theoretical prediction for the Pauli blocking probability by solving the integral (18) for the Fermi–Dirac distribution. The probability p_{Pauli} that two classically colliding fermions will indeed scatter is then given by the ratio of γ_{block} to this integral.

To find the optimal value of Δt for each system, we measure the collision rate in the absence of Pauli blocking for decreasing values of the time step and compare it to the theoretical prediction. The time step is small enough when we reach good agreement. It is important to switch off Pauli blocking for tuning the time step, as in the presence of Pauli blocking the collision rate is sensitive to the values of the smearing widths, which can obscure the inaccuracies due to a time step that is too large. After having found the optimal time step we check that repeated (unphysical) collisions of the same particle pair are rare. This has always been found to be the case with our collisional setup. We then use this optimal value for Δt to establish the optimal values of the smearing widths. We first identify the allowed interval for w_p and w_r given by conditions (15) and (16) and perform the same collision rate matching as described above, this time with Pauli blocking switched on. We find that the optimal widths lie between $w_r = w_p/(m\omega_0) = 1.0 l_{\text{ho}}$ for the lowest and $w_r = w_p/(m\omega_0) = 2.0 l_{\text{ho}}$ for the highest temperatures used in our analysis, where $l_{\text{ho}} = 1/\sqrt{m\omega_0}$ is the natural harmonic oscillator length unit.

The measured collision rates for the optimal choice of parameters with and without Pauli blocking together with the theoretical predictions are shown in figure 1. For sufficiently high temperatures the agreement is very good. At very low temperatures it becomes increasingly difficult to resolve conditions (15) and (16) for the Gaussian smearing widths simultaneously. For larger values of the scattering length this problem gets worse since test particles with a long relative distance can scatter on each other [7] and therefore the continuous distribution function needs to be resolved accurately over larger scales.

4.2. Equilibrium energy distributions

Another important test is to check that the system thermalizes to the correct equilibrium energy distribution, independently of the initial distribution. In the presence of Pauli blocking the energy is distributed according to the Fermi–Dirac distribution, whereas without Pauli blocking the particles will be distributed according to the Maxwell–Boltzmann distribution. Figures 2 and 3 show the results of this test for a low-temperature system with $|\tilde{k}_F a| = 1$ and isotropic trap frequencies. The parameter values for the time step and the smearing widths are optimal. We performed two tests of the thermalization. First we initialized the
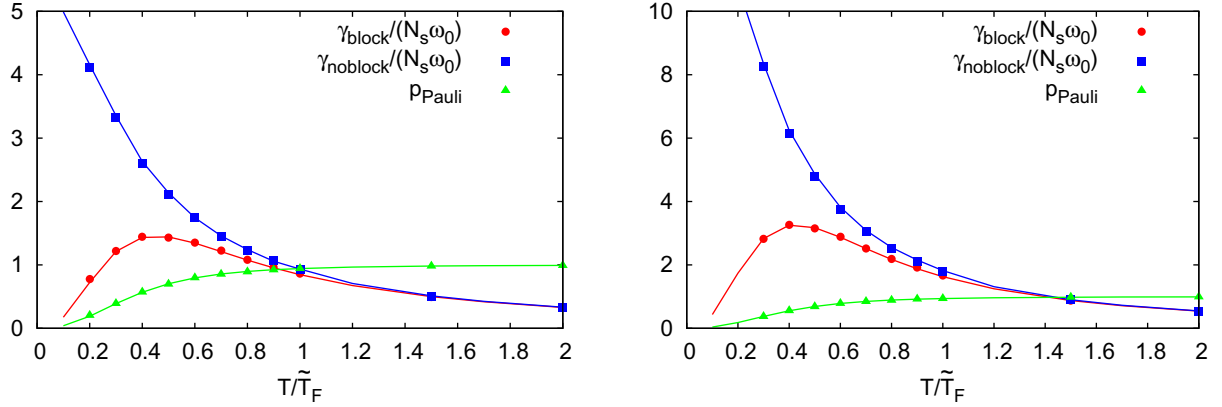
Figure 1. The equilibrium collision rates per particle (in units of ω_0) with and without Pauli blocking, as well as the Pauli probability for a successful scattering versus temperature for $|\tilde{k}_F a| = 1$ (left) and $|\tilde{k}_F a| = 2$ (right). The lines correspond to the theoretical prediction and the symbols to the values obtained with the simulation.

system according to the Fermi–Dirac distribution for $T = 0.2\tilde{T}_F$ (figure 2) and ran the simulation without Pauli blocking. After a short time, the system thermalized according to the Maxwell–Boltzmann distribution for $T = 0.31\tilde{T}_F$. Note that the temperatures of the two distributions are not necessarily equal, since the equipartition theorem does not hold for the Fermi–Dirac distribution. When changing from one distribution to the other the average energy of the system remains conserved and hence the temperature of the new equilibrium state is different. Figure 3 shows the corresponding results for the reverse situation: the initial distribution is Maxwell–Boltzmann with $T = 0.31\tilde{T}_F$ and Pauli blocking is switched on. It is clearly visible from both figures that the correct equilibrium distribution is always attained at the end of the simulation. This agreement improves further at higher temperatures.

4.3. Collective excitations

Collective excitations emerge when a many-particle system is perturbed away from equilibrium. Here, we will discuss three different excitation modes: the sloshing mode (also known as the dipole or Kohn mode), the breathing mode (monopole mode) and the quadrupole mode. We will confirm that the simulation gives the correct frequencies and damping properties of these modes. The following tests were performed for a spherical trap $\omega_x = \omega_y = \omega_z = \omega_0$.

The sloshing mode is excited by a small displacement of the centre of mass from its equilibrium position or equivalently by a short-lived force represented by an additional linear term in the potential. It is well known that the time evolution of each of the three centre of mass coordinates $\langle r_i \rangle$ is an undamped oscillation with the corresponding harmonic oscillator frequency ω_i. Figure 4 shows such an oscillation for a system at $|\tilde{k}_F a| = 1$ and $T = 0.2\tilde{T}_F$.

The breathing mode can be excited by compressing or expanding the cloud. In a spherical trap this yields an undamped oscillation of $\langle r^2 \rangle$ with frequency $2\omega_0$ around its equilibrium value [12]. Figure 5 illustrates this mode for a system with $|\tilde{k}_F a| = 1$ and $T = 0.2\tilde{T}_F$.

By perturbing the system via a short-lived small increase in one or several of the trap frequencies we can excite the quadrupole mode. We excite the quadrupole mode
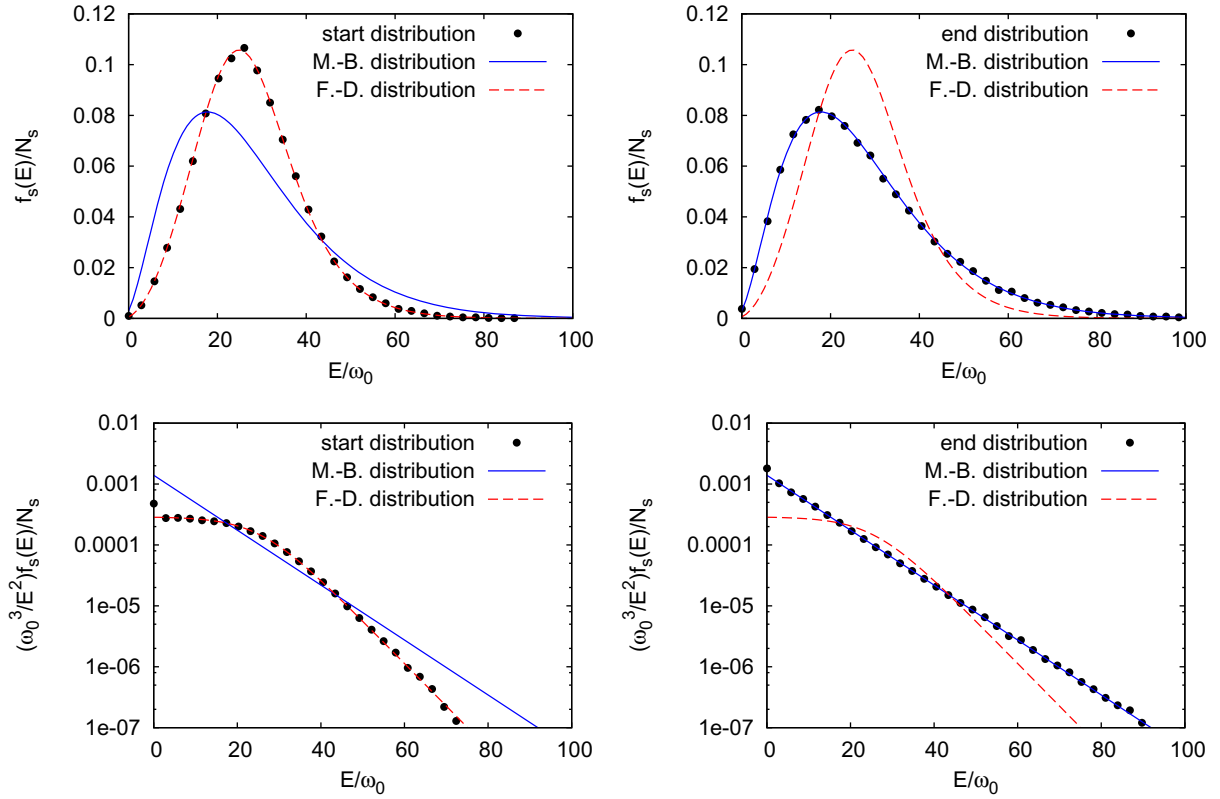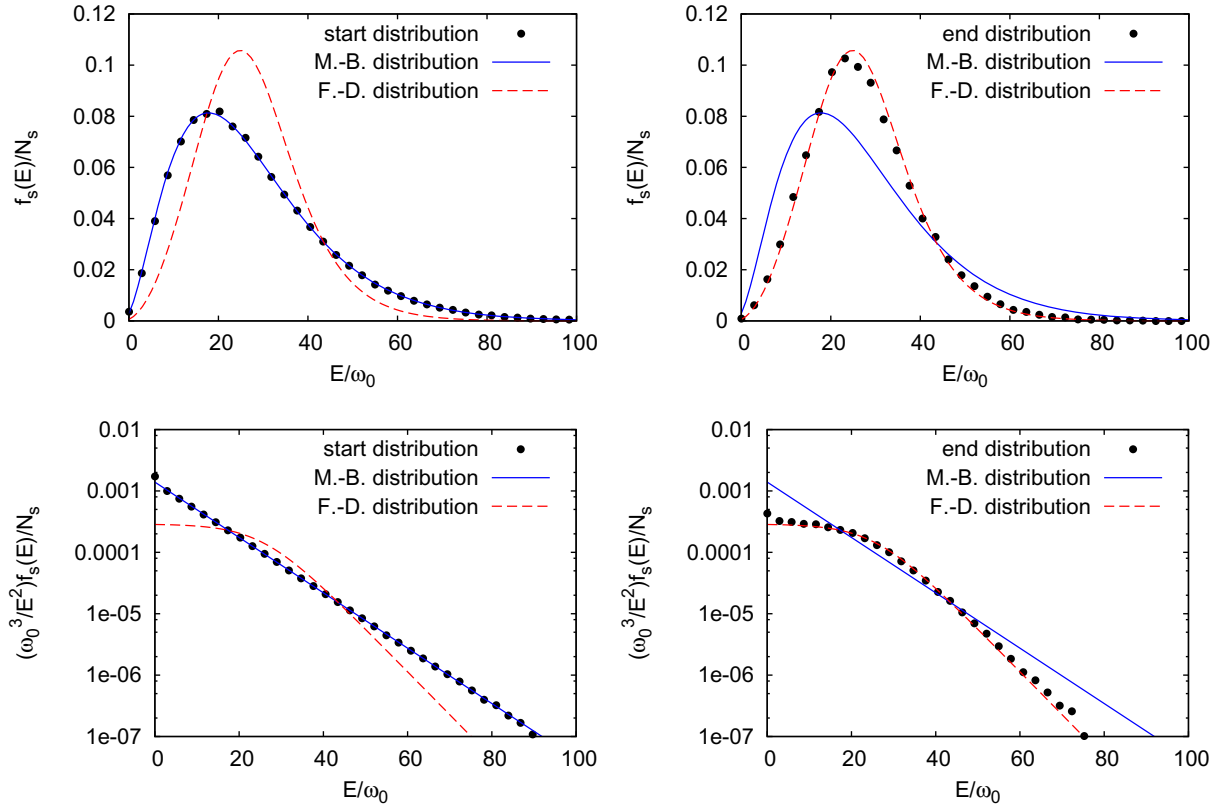
Figure 2. The equilibrium energy distributions without Pauli blocking. The top panel shows the energy distributions on a linear scale and the bottom panel shows the energy distributions scaled by ω_0^3/E^2 on a logarithmic scale. The start distribution (left) is Fermi–Dirac (F–D) at $T = 0.2\tilde{T}_F$ and the end distribution (right) is Maxwell–Boltzmann (M–B) with the same average energy but at $T = 0.31\tilde{T}_F$, as expected.

$Q(t) = \langle x^2 \rangle - \langle y^2 \rangle$ by applying the perturbation $\Delta p_x = -cx$ and $\Delta p_y = cy$ with $c = 0.2m\omega_0$ in the same way as in [7]. Unlike the sloshing and the breathing mode, this mode is damped. The frequency of the quadrupole mode at high temperatures approaches the ideal gas value $2\omega_0$, while at low temperatures it is closer to the hydrodynamic frequency $\sqrt{2}\omega_0$. Figure 6 shows the quadrupole mode for $|\tilde{k}_F a| = 1$ in the high- and low-temperature regimes. In both cases the damping of the mode is clearly visible. The frequency of the oscillation can be extracted from the corresponding Fourier transform $Q(\omega) = \int_0^\infty dt\, Q(t)e^{i\omega t}$ and is in agreement with the theoretical prediction, while the damping can be extracted from its imaginary part. We find that the damping is stronger at the lower temperature $T = 0.4\tilde{T}_F$ when collisions are more frequent (see figure 1 for a plot of the collision rate).

4.4. Comparison of different collisional setups

To study the impact of the collisional setup on the outcome of the simulation, we have implemented the setups 3.1 (angular momentum-preserving) and 3.2 (energy-preserving) and confirmed that they generate the same results for both the equilibrium and non-equilibrium

Figure 3. The equilibrium energy distributions with Pauli blocking. The top panel shows the energy distributions on a linear scale and the bottom panel shows the energy distributions scaled by ω_0^3/E^2 on a logarithmic scale. The start distribution (left) is Maxwell–Boltzmann (M–B) at $T = 0.31 \tilde{T}_F$ and the end distribution (right) is Fermi–Dirac (F–D) with the same average energy but at $T = 0.2 \tilde{T}_F$, as expected.

systems. First we analyse the magnitude of the changes in total energy (kinetic plus the trapping potential) with the angular momentum-conserving setup. Figure 7 shows a typical histogram of the relative change of energy of a particle pair $\Delta E/E_{\text{init}} = (E_{\text{final}} - E_{\text{init}})/E_{\text{init}}$ after a successful collision. The histogram is sharply peaked around zero. In this typical example, the majority of the collisions (approximately 84%) conserve the energy of the colliding pair with an accuracy of up to $|\Delta E/E_{\text{init}}| \leqslant 10^{-4}$. Since collisions are frequent and the energy changes have random sign we also observe large cancellation effects, such that the total energy of the system is conserved with an accuracy of the order of 10^{-7} at any given time. This is smaller than, for instance, the energy deviations due to Verlet's algorithm quoted in [7].

To understand the good accuracy of energy conservation we also make a qualitative theoretical estimate. During the collision the kinetic energy is conserved, such that it is sufficient to consider the potential energy V of the two particles,

$$V = \frac{m}{2} \left[\omega_\perp^2 \left(x_1^2 + y_1^2 + x_2^2 + y_2^2 \right) + \omega_z^2 \left(z_1^2 + z_2^2 \right) \right], \tag{20}$$

where (x_i, y_i, z_i) are the coordinates of the particle i and $\omega_\perp = \omega_x = \omega_y$ is the radial trap frequency. We can recast this expression in terms of the centre of mass and the relative
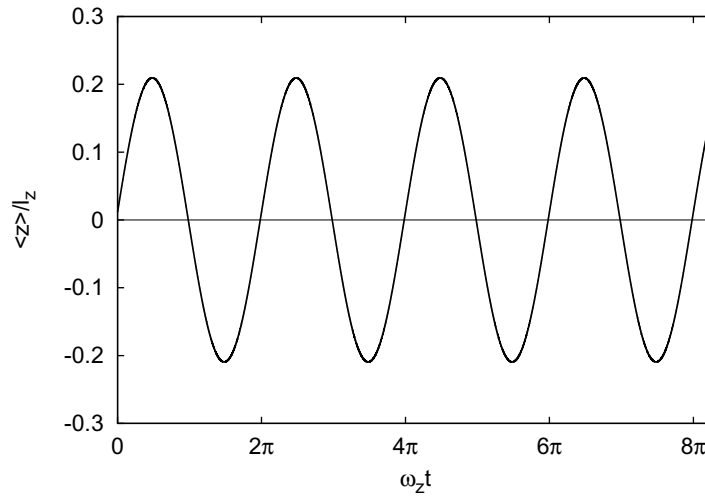
Figure 4. Simulation of the equilibrium sloshing mode $\langle z \rangle / l_z$, where $l_z = 1/\sqrt{m\omega_z}$. The mode is undamped and the oscillation frequency is equals to ω_z.
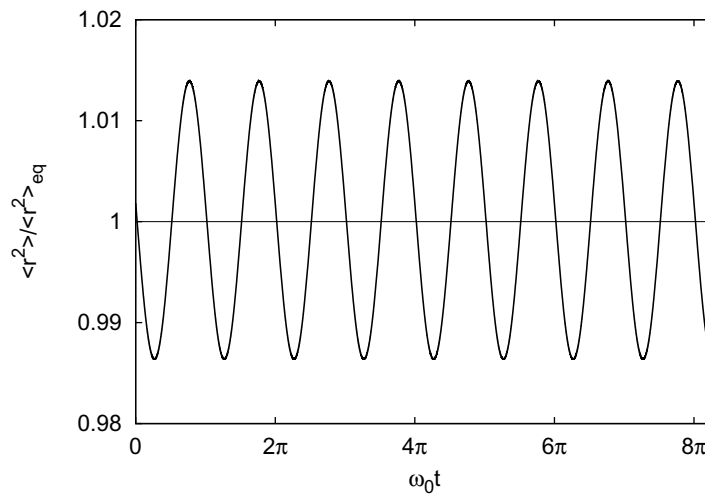
Figure 5. Simulation of the normalized equilibrium breathing mode $\langle r^2 \rangle / \langle r^2 \rangle_{\text{eq}}$. The breathing mode is undamped and the oscillation frequency is equals to $2\omega_z$.

coordinates (X, Y, Z) and (x, y, z), respectively,

$$V = m \left[\omega_\perp^2 (X^2 + Y^2) + \omega_z^2 Z^2 \right] + \frac{m}{4} \left[\omega_\perp^2 (x^2 + y^2) + \omega_z^2 z^2 \right]. \tag{21}$$

The position of the centre of mass is not affected by the collision. The variation in energy is, thus, only due to the contribution of the relative motion V_{rel}, defined by

$$V_{\text{rel}} = \frac{m}{4} \left[\omega_\perp^2 (x^2 + y^2) + \omega_z^2 z^2 \right]. \tag{22}$$

We now define a second frame (x', y', z') such that the z'-axis is parallel to the relative angular momentum **L** of the pair. In addition, since the trap is rotationally invariant around z, we can choose the initial coordinate system such that **L** is in the (x, z)-plane, in which case $y' = y$.
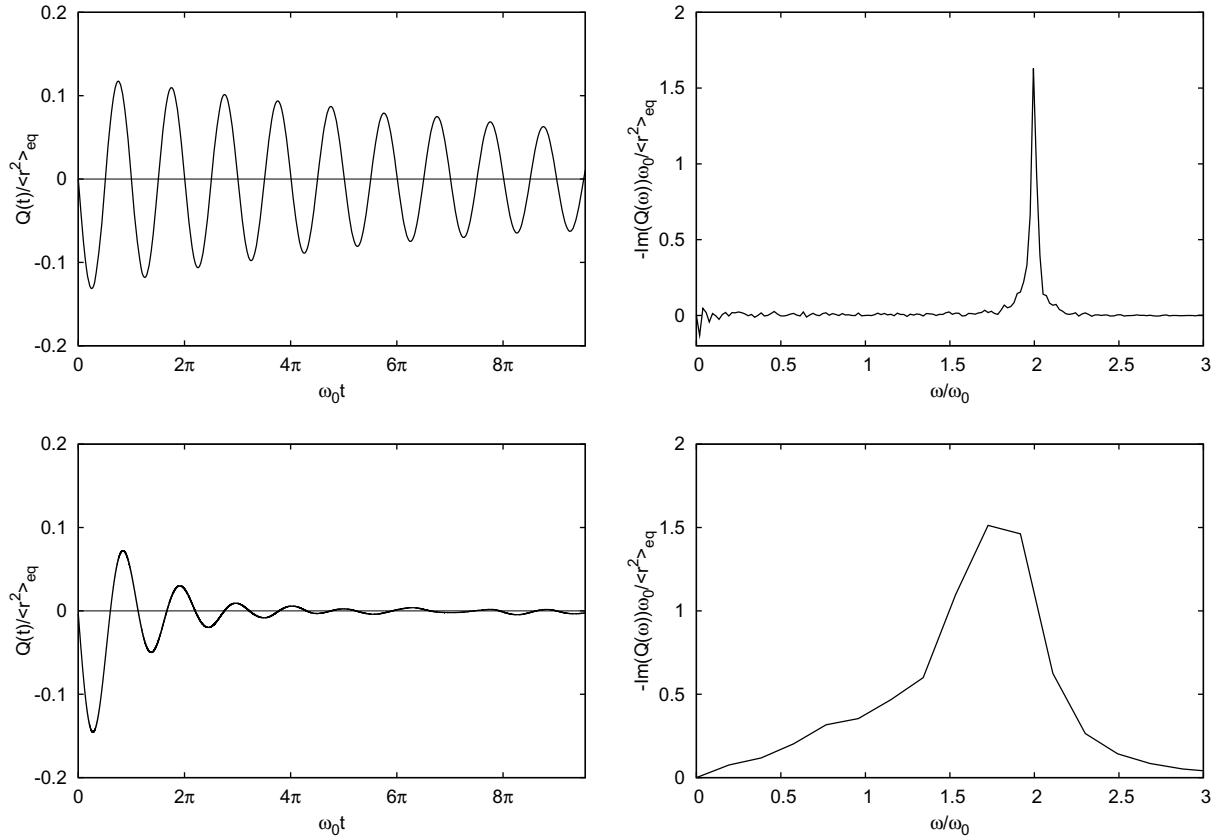
Figure 6. Left: simulation of the normalized equilibrium quadrupole mode $Q(t)/\langle r^2 \rangle_{\text{eq}}$ at high temperature $T = 2\tilde{T}_{\text{F}}$ (top panel) and at low temperature $T = 0.4\tilde{T}_{\text{F}}$ (bottom panel). Right: the imaginary part of the corresponding Fourier transforms of the numerical data gives information about the oscillation frequency and the damping.

If θ is the angle between $\mathbf{L}$ and the z-axis, the two sets of coordinates are related by the following relations:

$$x = x' \cos \theta + z' \sin \theta, \tag{23}$$

$$y = y', \tag{24}$$

$$z = z' \cos \theta - x' \sin \theta. \tag{25}$$

By conservation of angular momentum, the relative coordinates evolve in the (x', y')-plane. We thus have $z' = 0$, $x' = d \cos \varphi$ and $y' = d \sin \varphi$, where d is the relative distance between the two particles. In terms of d and φ, the relative potential energy is

$$V_{\text{rel}} = \frac{m\omega_\perp^2 d^2}{4} + \frac{md^2}{4} \left(\omega_z^2 - \omega_\perp^2 \right) \sin^2 \theta \cos^2 \varphi. \tag{26}$$

During the collision d and θ are conserved. The variation of energy is thus only due to the rotation in the (x', y') and we obtain

$$\Delta E = \frac{md^2}{4} \left(\omega_z^2 - \omega_\perp^2 \right) \sin^2 \theta \left[\cos^2 \varphi_{\text{f}} - \cos^2 \varphi_{\text{i}} \right], \tag{27}$$
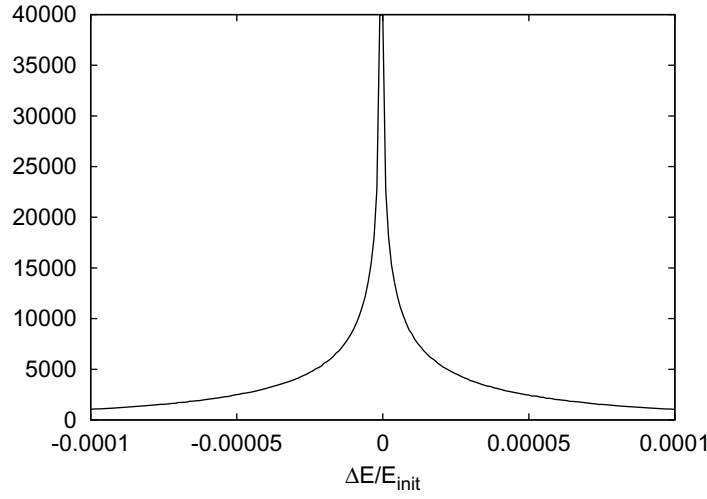
Figure 7. Probability density (obtained from the corresponding normalized histogram) for the relative change in energy of a colliding particle pair $\Delta E/E_{\text{init}} = (E_{\text{final}} - E_{\text{init}})/E_{\text{init}}$ for $|\tilde{k}_{\text{F}}a| = 1$, $T = 0.4\tilde{T}_{\text{F}}$, $\omega_\perp/\omega_z = 100$ and $\tilde{N} = 10N = 100\,000$.

where φ_{i} and φ_{f} correspond to the initial and final values of φ respectively. As an approximation, we normalize to the average total energy of the pair, $\bar{E} \approx 6T$, and obtain

$$\frac{\Delta E}{\bar{E}} = \frac{md^2}{24T} \left(\omega_z^2 - \omega_\perp^2\right) \sin^2 \theta \left[\cos^2 \varphi_{\text{f}} - \cos^2 \varphi_{\text{i}}\right]. \tag{28}$$

As shown above the distance between the particles can be at most $d_{\text{max}} = 2a\sqrt{N/\tilde{N}}$. Hence, for the range of parameters considered in this study the constant prefactor is of the order of $\lesssim 10^{-4}$. The trigonometric functions further reduce the variation of the energy and are responsible for the pointed shape of the histogram. Note that the method of test particles is important for a small energy variation. Due to $\tilde{N}$ being larger than N, the cross section and hence the average distance between two scattering partners are reduced, which leads to a smaller $\Delta E/E_{\text{init}}$ (in our case by a factor of $\tilde{N}/N = 10$). To demonstrate this effect, figure 8 shows the variance of the energy change as a function of the ratio $\tilde{N}/N$. The data are well fitted by a line with slope -2 on a double-logarithmic scale, which confirms relation (28). Analogous scaling laws can also be shown for the dependence on temperature and scattering length.

We also compared the time evolutions of the centre-of-mass coordinates in response to a perturbation. The differences between the two setups were found to be smaller than the statistical fluctuations. Taking these results into account we conclude that the two setups 3.1 and 3.2 are equivalent on a macroscopical scale and we have the freedom to choose whichever option appears more convenient.

We adopt the angular momentum-conserving setup 3.1, not only because of this property, but also since the setup from [7] has a small technical disadvantage. Since the new direction of the relative momentum vector is chosen uniformly on a sphere, in many cases the particles are found to approach each other again after a successful collision. This implies that in the following time step they are likely to undergo another collision. The proportion of such events compared to the total number of collisions can reach up to 40% at the lowest temperature considered
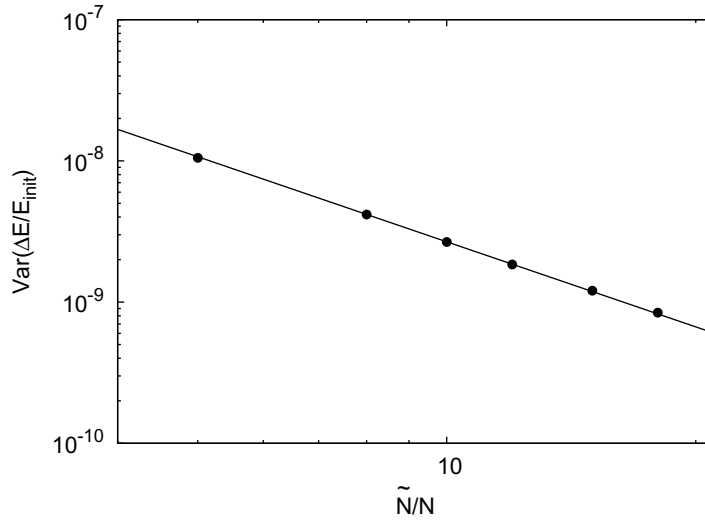
Figure 8. Double-logarithmic plot of the variance of the energy change during a collision $\mathrm{Var}(\Delta E/E_{\mathrm{init}})$ for $|\tilde{k}_{\mathrm{F}}a| = 1$, $T = \tilde{T}_{\mathrm{F}}$ and $\omega_\perp/\omega_z = 100$ as a function of the test particle to particle ratio $\tilde{N}/N$. The line corresponds to a linear fit with constant slope -2 on the double-logarithmic scale.

in this study and amounts to about 10% at $T = \tilde{T}_{\mathrm{F}}$. To avoid this overcounting of collisions one needs to implement an additional routine that prevents particles from colliding with each other repeatedly within short time intervals. In other words the molecular chaos assumption does not hold with the setup from [7] and needs to be enforced artificially. In our setup repeated scattering is so rare that this effect can be neglected. This is because the relative position and the relative momentum vectors of the particle pair are rotated by the same random angle and hence their relative angle is preserved. After a collision takes place the particles continue to move on trajectories that diverge from each other.

4.5. Outlook

In addition to the two collisional setups described above, we propose a third very general collisional setup which can be explored in future work.

To preserve macroscopical averages we keep the centre-of-mass coordinates and momentum fixed and we work with the six degrees of freedom for the relative momentum and position. Based on the idea of a delocalized particle pair, we assume that the relative phase space coordinates of the particles are distributed according to a Gaussian. We then choose the new relative position and momentum randomly according to the Gaussian probability distribution with the additional constraints given by the symmetries of the problem. Energy and L_z conservation, for instance, reduce the problem by two degrees of freedom. If the energy and total angular momentum are conserved, the problem is reduced by four degrees of freedom and so on.

It is important to stress, however, that the task of defining a probability measure on a complicated hypersurface in the phase space (in our case defined by the constraints of energy and angular momentum conservation) is a mathematically highly non-trivial problem and will pose a challenge for the numerical implementation.

5. Conclusion

We have implemented a Boltzmann equation approach to the simulation of the semiclassical regime of two-component Fermi gases. We described how to implement the method using test particles and stressed the advantages of the auxiliary grid. We also presented an extensive range of tests for the simulation. The main focus of this work was on a discussion of the different possibilities for implementing collisions, namely the angular momentum-conserving and the energy-conserving setups. We studied in detail the error in energy of the former scheme and showed that it is indeed very small, so that it becomes a valid alternative way of calculating the collisional integral and has distinct advantages since it minimizes repeated scattering events.

Strictly speaking, the validity range of the Boltzmann equation is limited to the high-temperature, dilute regime where many-body correlations can be safely neglected. In future work, we will introduce a Hartree term that will mimic the real equation of state of the cloud, as obtained recently both experimentally and theoretically. This will allow us to describe the density profile of the cloud more accurately. We also intend to apply the method to systems with components of unequal mass which bring a greater variety of dynamical regimes and which can provide a more stringent test of the Boltzmann equation approach to these systems.

Acknowledgments

References

[1] Inguscio M, Ketterle W and Salomon C (ed) 2006 *Proc. Int. School of Physics 'Enrico Fermi' on Ultracold Fermi Gases, Course CLXIV, Varenna* (Società Italiana di Fisica)
[2] Sommer A, Ku M, Roati G and Zwierlein M W 2011 *Nature* **472** 201–4
[3] Sommer A, Ku M and Zwierlein M W 2011 *New J. Phys.* **13** 055009
[4] Trenkwalder A, Kohstall C, Zaccanti M, Naik D, Sidorov A I, Schreck F and Grimm R 2011 *Phys. Rev. Lett.* **106** 115304
[5] Cao C, Elliott E, Joseph J, Wu H, Petricka J, Schaeer T and Thomas J E 2010 *Science* **331** 58
[6] Goulko O, Chevy F and Lobo C 2011 *Phys. Rev.* A **84** 051605
[7] Lepers T, Davesne D, Chiacchiera S and Urban M 2010 *Phys. Rev.* A **82** 023609
[8] Goulko O 2011 Thermodynamic and hydrodynamic behaviour of interacting Fermi gases *PhD Thesis* University of Cambridge
[9] Uehling E A and Uhlenbeck G E 1933 *Phys. Rev.* **43** 552–61
[10] Jackson B and Zaremba E 2002 *Phys. Rev.* A **66** 033606
[11] Wade A C J, Baillie D and Blakie P B 2011 *Phys. Rev.* A **84** 023612
[12] Guéry-Odelin D, Zambelli F, Dalibard J and Stringari S 1999 *Phys. Rev.* A **60** 4851–6